Radiation Assessment of a 56-Gb/s Electro-Absorption Modulator Driver for Optical Intrasatellite Links

Kieran De Bruyn, *Student Member, IEEE*, Arijit Karmakar, *Member, IEEE*, Warre Geeroms, Michael Vanhoecke, Laurens Bogaert, Günther Roelkens, *Senior Member, IEEE*, Alan Naughton, David Mackey, Jeffrey Prinzie, *Member, IEEE*, Paul Leroux, *Senior Member, IEEE*, and Johan Bauwelinck, *Senior Member, IEEE*

***Abstract*— This article presents a radiation-hardened-by-process 56-Gb/s electro-absorption modulator (EAM) driver designed in a 130-nm silicon germanium (SiGe) bipolar complementary metal oxide semiconductor (BiCMOS) technology for application in optical intrasatellite links. Details of the driver architecture are provided, along with the electrical and optical measurement setups used to evaluate its performance. To assess the vulnerability of the driver against radiation exposure in the space environment, samples were irradiated with X-rays up to a total accumulated dose of 1.2 Mrad(Si), simulating the effects of total ionizing dose (TID) in orbit. Furthermore, heavy-ion experiments corroborated the driver's resilience to single-event transients (SETs) across a range of linear energy transfers (LETs) from 20 to 65.2 MeV cm^2/mg, with a particle fluence of 1.2 × 10^7 cm^{-2}. No single-event latchup (SEL) was observed in the irradiated samples during the heavy-ion exposure.**

***Index Terms*— Analog integrated circuit (IC) design, optical transmitters, radiation effects, radiation hardening by process.**

I. Introduction

TERRESTRIAL short-reach optical communication links have consistently achieved speeds greater than 100 Gb/s for quite some time now [1], [2], [3] due to continuous advancements in photonic devices, optical fiber technology, signal processing, and modulation techniques. These technological advances, in addition to the growing demand for high-speed data transmission to support increased Internet traffic and data center interconnects, have proved the feasibility and reliability of these links operating beyond 100 Gb/s. An emerging trend in the satellite industry is to use these relatively mature terrestrial optical communications technologies in place of the bulky waveguide-based radio frequency (RF) interfaces that currently manage intersatellite and intrasatellite communications links for, for example, onboard digital signal processors and science instruments [4]. The adoption of optical interfaces, and, more recently, the integration of photonic circuits, translates into significant reductions in terms of size, weight, and power (SWaP) of onboard equipment compared to conventional purely electrical RF transceivers because the heavy metal waveguides can be replaced with lightweight optical fiber. This ultimately leads to cost-effective and power-efficient versatile satellite payloads.

The severe space-radiation environment [5], [6], [7], [8], illustrated in Fig. 1, presents a significant challenge for the reliable operation of electronic and optical communication interfaces on satellites and spacecraft. The activity of the Sun significantly modulates the terrestrial radiation environment around the Earth in space with short- and long-term fluctuations along with the phase of the solar cycle. Beyond the Earth's protective atmosphere, the principal amount of ionizing radiation in space originates from galactic cosmic rays (heavy ions and high-energy protons), solar flares and emissions (low-energy protons and magnetic flux), and the Van Allen radiation belt, which contains the trapped charged particles [9], [10]. Near geosynchronous orbits (GEOs), the primary risk for

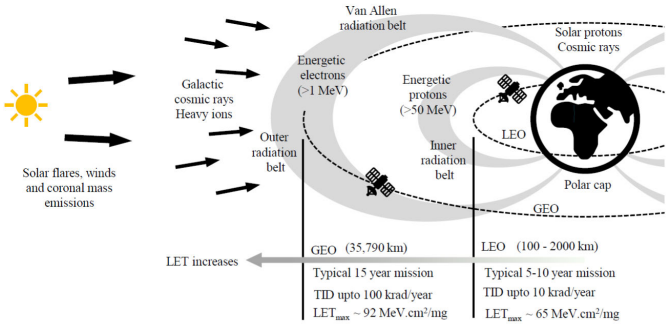

Fig. 1. Hazardous space-radiation environment around the Earth in space.

Received 12 December 2024; revised 21 January 2025 and 10 February 2025; accepted 14 February 2025. Date of publication 19 February 2025; date of current version 18 April 2025. This work was supported in part by the European Space Agency (ESA) project ProtoBIX under Contract 4000130531/20/NL/AR, in part by MBRYONICS Ltd., and in part by the Research Foundation Flanders (FWO) under Grant 1SF3523N. *(Corresponding author: Kieran De Bruyn.)*

Kieran De Bruyn, Arijit Karmakar, Warre Geeroms, and Johan Bauwelinck are with IDLab, Department of Information Technology, Ghent University-imec, 9052 Ghent, Belgium (e-mail: kieran.debruyn@ugent.be).

Michael Vanhoecke was with IDLab, Ghent University-imec, 9052 Ghent, Belgium. He is now with NVIDIA, 9000 Ghent, Belgium.

Laurens Bogaert and Günther Roelkens are with the Photonics Research Group, Ghent University-imec, 9052 Ghent, Belgium.

Alan Naughton and David Mackey are with MBRYONICS Ltd., Galway, H91 XK22 Ireland.

Jeffrey Prinzie and Paul Leroux are with the Department of Electrical Engineering, KU Leuven, 2440 Geel, Belgium.

Color versions of one or more figures in this article are available at https://doi.org/10.1109/TNS.2025.3543637.

Digital Object Identifier 10.1109/TNS.2025.3543637

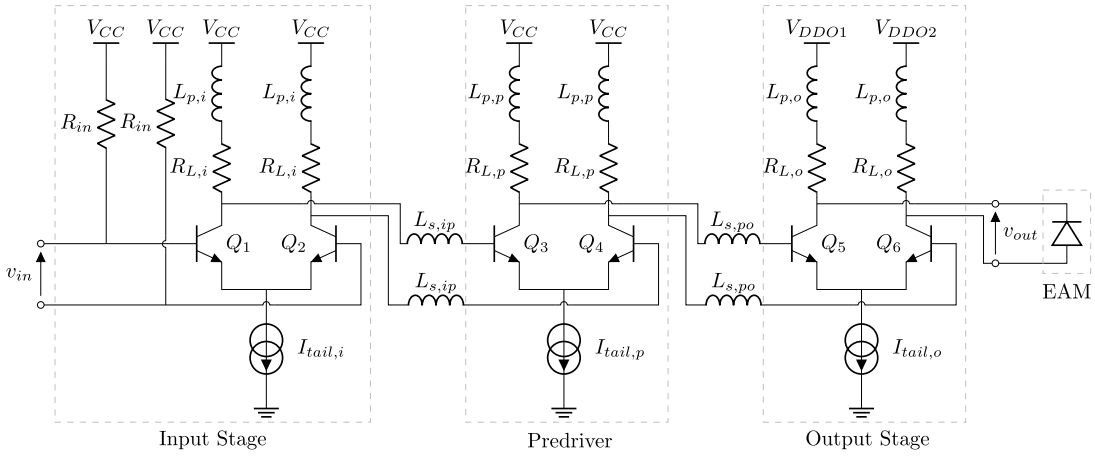

Fig. 2. Simplified schematic of a single channel of the proposed driver, ESD protection circuitry, and corresponding matching networks omitted. The EAM will be implemented on a separate PIC. For the EAM to be biased correctly in the pictured orientation, $V_{\mathrm{DDO1}} > V_{\mathrm{DDO2}}$.

satellites and spacecraft arises from heavy-ion-rich galactic cosmic rays and high-energy solar particles, which cause single-event effects (SEEs) like single-event upsets (SEUs) and single-event transients (SETs) in onboard components. The outer zone of the Van Allen radiation belt is dominated by energetic electrons, leading to total ionizing dose (TID) and displacement damage (DD). Typically, TID levels can accumulate up to 100 krad/year in this region [11], necessitating multi-Mrad(Si) radiation-hardened satellite components. Although the impact of TID can be mitigated with an adequate shielding thickness, shielding is not effective in significantly reducing the impact of high-energy particles causing SEEs. The satellites in a low Earth orbit (LEO) are primarily affected by high-energy trapped protons in the inner zone of the Van Allen radiation belt and there the TID levels can accumulate up to 10 krad/year [11]. For reliable operation, the LEO satellites necessitate an SEE and single-event latchup (SEL) tolerance up to a linear energy transfer (LET) of 60–65.2 MeV cm^2/mg which extends to an LET of 90–100 MeV cm^2/mg for GEO satellites [12] and interplanetary space missions.

Currently, optical transceivers on satellites utilize optical technologies that are restricted to 12.5 Gb/s per lane [12], [13], [14]. However, ongoing development efforts are targeted to achieve significantly higher line rates exceeding 25 or even 56 Gb/s with newer high-speed radiation-hardened-by-process technologies such as silicon germanium (SiGe) or fully depleted silicon on insulator (FDSOI) [15], [16], [17], [18]. Typically, as technology has scaled toward advanced nodes, the variations induced by TID tend to improve, while sensitivity to SEEs worsens [19], [20]. SiGe-based technologies are suitable for space applications considering their multi-Mrad(Si) immunity [15], however, the SEEs are a concern in heavy-ion-rich environments [21], [22]. Compared to electronic components, the optical or integrated photonic devices are experimentally found to be hardened up to multi-Mrad(Si) TID levels [23], [24], [25], [26]. Recently, the propagation of SETs from the electrical domain to the photonic domain has been investigated, revealing potential impacts on data integrity in photonic interfaces. However, these occurrences can be mitigated by employing SEE-tolerant drivers [27].

The work presented in this article focuses on the optical modulator driver for radiation-hardened optical communication links. While radiation-hardened vertical-cavity surface-emitting laser (VCSEL) drivers [28], [29], [30], [31], [32], Mach–Zehnder modulator (MZM) drivers [33], [34], [35], [36] and a microring modulator (MRM) driver [35] have been reported before, the targeted speed per channel of 56 Gb/s is 1.4 times that of previously reported radiation-hardened drivers. To the authors' knowledge, this makes this design the fastest radiation-hardened optical modulator driver reported thus far.

II. Optical Modulator Driver Design

The proposed optical transmitter comprises a silicon photonic integrated circuit (PIC) with C-band SiGe electro-absorption modulators (EAMs) and a SiGe bipolar complementary metal oxide semiconductor (BiCMOS) driver integrated circuit (IC) which provides an appropriate bias and modulation voltage to the EAMs. EAM- and MRM-based transmitters generally consume significantly less power compared to MZMs [37], [38]. EAMs and MRMs induce a higher chirp to the optical carrier compared to MZMs, however, for intrasatellite links of a few meters long, the resulting dispersion is negligible [39], [40]. Both EAMs and MRMs provide sufficient bandwidth (>50 GHz) [39], [40], but MRMs are more sensitive to temperature and wavelength variations and require accurate real-time wavelength locking which again increases the total power consumption of the transmitter [39], [40], so EAMs were selected as the appropriate modulator.

The EAM driver was implemented in a radiation-assessed SiGe 130-nm BiCMOS process, whose heterojunction bipolar transistors (HBTs) were found to withstand TIDs of 800 krad(Si) [41]. SiGe HBTs excel in high-speed analog and mixed-signal circuits, making them ideal for applications like the EAM driver, where high data rates are essential. Compared to CMOS, SiGe HBTs offer better speed, gain, and low noise at high frequencies, which are critical for telecom and datacom applications.

However, radiation hardening poses a challenge: techniques like enlarging transistors or using enclosed layouts

increase parasitic capacitance, slowing circuit operation and limiting high-frequency performance. This tradeoff becomes even more significant in radiation-sensitive environments like space, nuclear, terrestrial applications, and high-energy physics experiments, where reliability must be prioritized over speed. Balancing these conflicting demands remains a key challenge in designing circuits that are both radiation-resistant and capable of supporting high-speed communication. A more in-depth discussion of these tradeoffs will follow at the end of this section.

A simplified schematic of the design can be found in Fig. 2, where electrostatic discharge (ESD) protection circuitry and the corresponding matching networks were omitted. The design consists of a cascade of three differential gain stages with shunt peaking inductors $L_{p,i}$, $L_{p,p}$, and $L_{p,o}$ [42]. The three stages are connected to each other with series peaking inductors $L_{s,\mathrm{ip}}$ and $L_{s,\mathrm{po}}$ to boost the electrical 3-dB bandwidth of the driver. The output stage drives a silicon photonic (SiPh) EAM differentially, as in [43]. The two branches of the output stage receive a different supply voltage, V_{DDO1} and V_{DDO2}, to properly reverse bias the EAM.

The tail current sources are derived from a single current reference input using feedback-assisted current mirrors as shown in Fig. 3. This topology was chosen to obtain a low output compliance voltage to minimize the required supply voltage and thus limit the power consumption.

In addition to the inherent TID resistance of the SiGe HBTs, care was taken to further enhance radiation hardness, particularly against SEEs such as transients and latchups, which are harder to mitigate in high-speed designs. Including digital control circuitry on the high-speed application specific integrated circuit (ASIC) adds potential points of failure due to radiation influence and should be avoided where possible. As such, digital equalization techniques or digital calibration blocks to compensate for variations are not present. Additionally, no switchable photocurrent sinking sources as in [43] are implemented. Instead, the output stage and its tail current source are designed to absorb the photocurrent expected from the SiPh EAM. This way, vulnerability to SEE-induced digital errors of the design is significantly reduced.

Additionally, to avoid latchup originating from radiation sources, neighboring nMOS and pMOS transistors in the current biasing circuitry are separated with double guard rings [44]. While this is a standard SEE mitigation technique, it was essential to further improve the radiation tolerance of the design, while keeping its high-speed performance acceptable.

As explored in [45], a reliable way to increase the radiation hardness of a current mode logic (CML) SiGe-HBT design without sacrificing high-speed performance is to increase the hardness of the dc current source. In the case of this design, this has been done by incorporating external negative feedback. To gauge the effect of SETs in this tail current source, some SPICE simulations were performed by modeling the SETs by the double-exponential current model of (1) [46], [47], where $I_{\mathrm{inject}}(t)$ defines the current pulse caused by collecting a charge Q_{charge}. τ_f defines the fall time of the pulse, while τ_r defines the rise time. Both these parameters are heavily technology-dependent. As such, in the simulation, these time constants are taken from a similar 130-nm CMOS

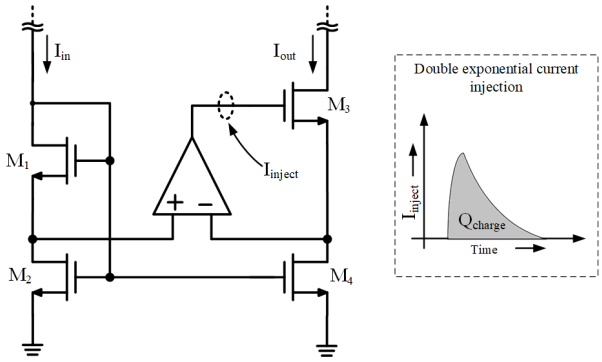

Fig. 3. Biasing tail current mirror circuit with the sensitive node used for SET simulation using a double exponential current with injected charge Q_{charge}.

technology [48] from the same vendor, specifically $\tau_r = 10$ ps and $\tau_f = 100$ ps

$$I_{\mathrm{inject}}(t) = \frac{Q_{\mathrm{charge}}}{\tau_f - \tau_r}\left(e^{-\frac{t}{\tau_f}} - e^{-\frac{t}{\tau_r}}\right). \tag{1}$$

In this way, one critical point was identified. To achieve a sufficiently high output impedance in the feedback-assisted biasing current mirror, the current in the output branch of the op-amp is fairly low. In the event of a strike of a charged particle on this node, a current transient in the output branch will be generated. Because of the low current in this branch, this node is extra sensitive to this disruption, which will affect the gate voltage of M_3. To simulate this effect, double exponential current transients with an equivalent charge of 1 and 10 pC are injected into the output node of the op-amp. According to [48] and [49], this approximately matches an LET of 1–10 and 10–100 MeV cm^2/mg, respectively, depending on the exact collection depth. During the simulation, the node voltage and the output of the driver are monitored. The result can be seen in Fig. 4(a), where it is clear that after 5 ns, there is still a considerable voltage difference at the output node of the op-amp. This will thus affect the emitter voltage of the HBTs. In the branch of the differential pair with the lower supply voltage, the collector–emitter voltage V_{CE} of the HBT is already limited compared to the branch with the higher supply voltage. The decreased V_{CE} resulting from the additional voltage at the output of the op-amp of the current source will thus make that transistor move closer to the saturation region. The more this effect takes place, the more f_T of the transistor will decrease [50], which corresponds to a slower rise time. This can be seen in Fig. 4(b) and is further confirmed by the fact that the slower transitions move from the rising edges to the falling edges when V_{DDO1} and V_{DDO2} are switched.

To conclude this section, the tradespace of a general radiation-hardened optical driver IC is explored. The main parameter that is determined by the designer of such a circuit is the current throughout the output stage. Increasing this parameter will have a fourfold effect: the driving voltage, determined in its simplest approximation by the internal termination resistor and Ohm's law, will increase. Naturally, the total power consumption of the driver will increase as well. Third, the bandwidth of the driver will reduce, as there is an optimal current associated with the maximal f_T of the HBTs. Finally, since the total current in the branches is higher, the

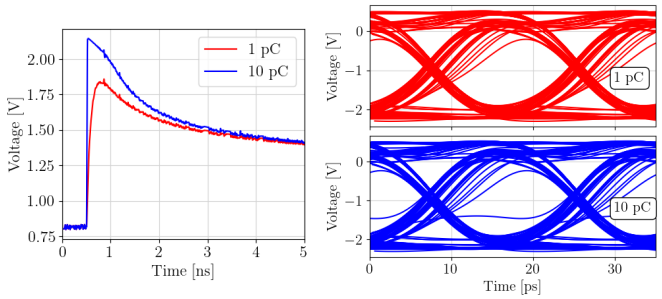

(a) (b)

Fig. 4. SET simulations of the critical node for the injected charge of 1 (red) and 10 pC (blue). (a) Node voltage. (b) Eye diagram at the output of the driver captured during the same 5-ns interval.

deviation by any current induced by a particle strike will have a relatively lower impact.

Some other parameters change when irradiating, the most impactful of which is the current gain of the HBT. However, since any good design using HBTs is robust against variations in current gain, this radiation-induced effect is inherently negated. In the case of this work, since the collector current in the output stage is fixed, a change in current gain β of the HBTs means a change in the base current. By making sure that the main current in the previous stage is large enough compared to the base current, no noticeable change occurs in the base bias voltage. For signal voltages, the fact that the output load of the previous stage is small compared to the input impedance of the transistors means that there is only a voltage signal transfer, the transfer of a current signal is too small to be considered. Other parameters like transit time, f_T, and $f_{\max}$ also degrade, but those values change only negligibly for the radiation levels considered in this work [51].

A final choice in the hands of a designer is the type of transistor with which to build the circuit. Other choices than the n-p-n HBTs used in this work could be p-n-p HBTs [22] or SiGe HBTs used in the inverse mode [52], which have shown to be more robust to TID effects and to have an improved SET response, respectively. However, both alternative choices are associated with lower achievable speeds, which is why they were not considered in this work.

III. Electrical and Optical Measurements

A micrograph of the fabricated die can be seen in Fig. 5. Initially, the electrical properties of the unirradiated driver were measured. The frequency response was measured by connecting a vector network analyzer (VNA) using RF probes to the sample as in Fig. 6(a). As shown in Fig. 7, for an input power of −5 dBm, the electrical 3-dB bandwidth was determined to be 39 GHz. The increasing bandwidth for high input powers is explained by the fact that the driver is only able to deliver a certain peak–peak output voltage, which is mostly limited by the supply voltage and the tail current. The gain predicted by a small-signal analysis (which corresponds to the low input power case) would put the output voltage over that limit when a large enough input voltage is applied. This will make the gain at lower frequencies effectively compress, which looks like the bandwidth expanding.

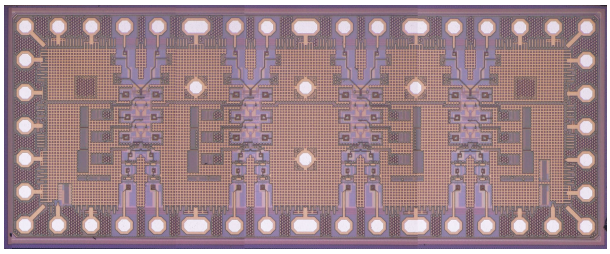

Fig. 5. Micrograph of the proposed driver chip (2720 × 1070 μm).

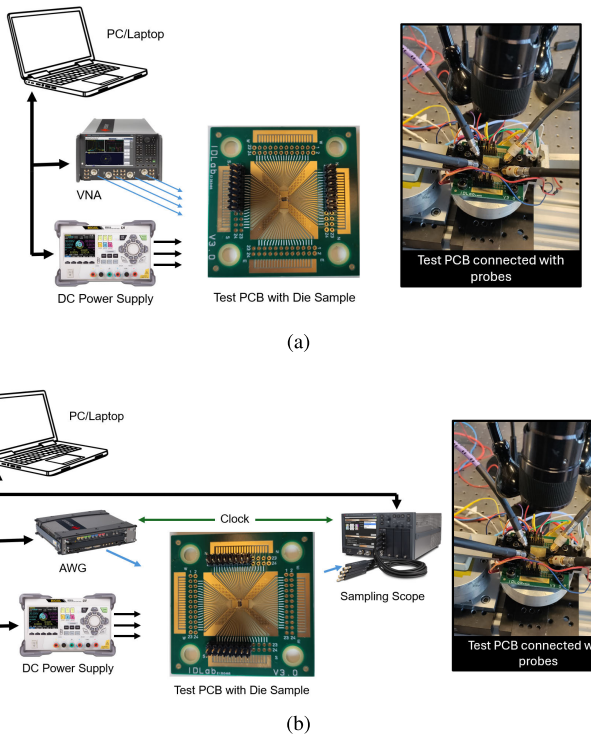

Fig. 6. Measurement setups for (a) VNA measurement and (b) electrical time-domain measurement.

The time-domain performance of the driver was tested by the setup of Fig. 6(b). A 92-GSa/s arbitrary waveform generator (AWG) was used to generate a 300-mVppd, 56-GBd nonreturn-to-zero (NRZ) pseudorandom bit sequence (PRBS)-13 signal. The driver was connected by RF probes. The output signal was then measured using a 256-GSa/s sampling oscilloscope. The eye diagram of this measurement can be seen in Fig. 8(a).

However, the load presented by the oscilloscope is 50 Ω on each measurement channel, while an EAM presents a purely capacitive load. Since the internal load resistors, $R_{L,o}$ in Fig. 2, are also 50 Ω, the output impedance thus effectively becomes 25 Ω. This will cause the output swing to double for the EAM compared to the electrical measurements on the scope since it is set by the current through the output impedance. The electrical measurements are summarized in Table I.

To analyze the unirradiated optical performance of the driver, it was put in a relatively simple optical test setup, as shown in Fig. 9. The driver IC and the PIC containing the EAM were mounted on a PCB and wire-bonded to each other as shown in Fig. 9(a). The co-designed PIC was fabricated

TABLE I
ELECTRICAL MEASUREMENTS

Specification	Value
Large signal electrical bandwidth	39 GHz
Differential output swing	1.5 Vppd
Output bias range	−1.5 to 1.5 V
Power consumption (4 channels)	250 mW
Power efficiency at 56 Gbps	1.1 pJ/b

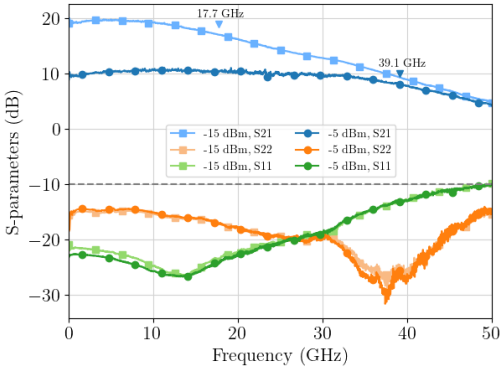

Fig. 7. Measured S-parameters. S_{dd21} in blue, S_{dd11} in orange, and S_{dd22} in green. Circle markers for input power of −15 dBm, whereas square markers for input power of −5 dBm. 3-dB bandwidth annotated.

on imec's iSiPP50G SiPh platform. A continuous-wave (CW) laser was coupled into a polarization controller and then into the PIC using a fiber array mounted on a dedicated alignment system. The same NRZ PRBS-13 input signal was supplied using a 92-GSa/s AWG connected with a TR-70 connector and PCB traces wire-bonded to the input bondpads of the driver. The AWG output signal was precompensated for the frequency-dependent losses in the cables and TR-70 connector. Since no dedicated transimpedance amplifier (TIA) was used, the optical output signal was amplified using a benchtop erbium-doped fiber amplifier (EDFA) before a 70-GHz reference photodiode connected to a 256-GSa/s sampling oscilloscope.

The driver can provide a 1.5-Vppd, 56-Gb/s signal to the EAM, which is biased near the point of optimal extinction ratio (ER) versus insertion loss (IL) tradeoff, or 1.3-V reverse bias ($V_{DDO1} = 2$ V and $V_{DDO2} = 3.3$ V) at a laser wavelength of 1530 nm. The resulting eye diagram measured at the output of the photodiode can be seen in Fig. 8(b). The ER reached was 2.4 dB and could be improved to 2.8 dB by increasing the bias voltage over the EAM to 1.5 V by increasing the greater of V_{DDO1} and V_{DDO2} to 3.5 V and slightly increasing the supply voltage from 1.2 to 1.3 V. This will evidently also increase the power consumption of the driver. However, a higher bit rate signal can now be transmitted, as shown in Fig. 8(c). The resulting power efficiency without accounting for the laser power is now 0.9 pJ/b.

IV. RADIATION CHARACTERIZATION

A. Total Ionizing Dose

The TID test was performed at KU Leuven, Geel campus, Belgium, using an X-ray source, with a spot size diameter of approximately 3 cm. The test setup is visible in Fig. 10(a). The X-ray beam is generated from a 23-keV, 15-mA W-tube.

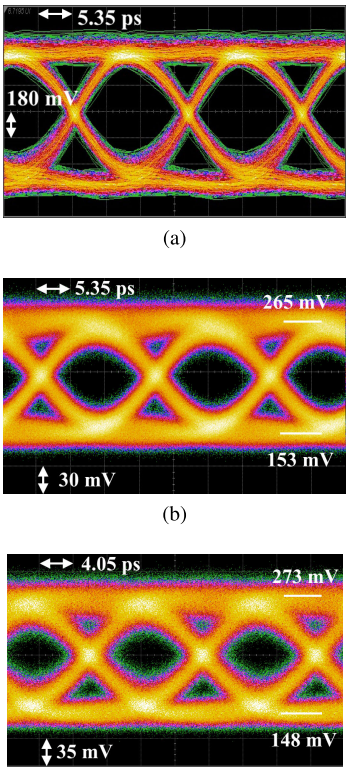

Fig. 8. (a) Electrical eye diagram for 56-Gb/s PRBS-13 NRZ. (b) Electro-optical eye diagram for 56-Gb/s PRBS-13 NRZ. (c) Electro-optical eye diagram for 74-Gb/s PRBS-13 NRZ with increased bias and supply voltage.

Before exposure of the sample to radiation, the X-ray beam's dose rate was calibrated using a p-i-n diode-based radiation detector. To emulate the LEO environment, multiple samples were exposed to a dose rate of 25 krad(Si)/h, for a total dose of 1.2 Mrad(Si) [53]. Since enhanced low-dose-rate sensitivity (ELDRS) is not present in SiGe-based HBTs [15], a slightly higher dose rate was chosen to cover a longer lifetime (>5 years) of the satellite with the test.

All devices were irradiated at room temperature while connected to the appropriate supplies. After irradiation, half of the samples were annealed for 24 h at ambient temperature, and the other half were put in a temperature-controlled chamber for seven days at 100 °C. Each annealing technique was tested with four samples, which means that in total, eight samples were tested.

The frequency response was measured with a Keysight P5028A VNA before and after irradiation, as well as during irradiation for the devices connected to the supply. The RF level applied to the inputs of the driver for this test is −5 dBm. The result is shown in Fig. 11, where it is clear that at 1.2-Mrad(Si) irradiation, there is only 0.1-dB difference in frequency response compared to the preirradiation measurement results. The measurements pre- and postirradiation were conducted on the entire package, including a TR70 connector and dedicated PCB. There is thus a difference in an achieved bandwidth of a few GHz compared to the results discussed in Fig. 7.

B. Single-Event Effects

The SEE tests were performed at the cyclotron of Université Catholique de Louvain, Louvain-la-Neuve, Belgium. The

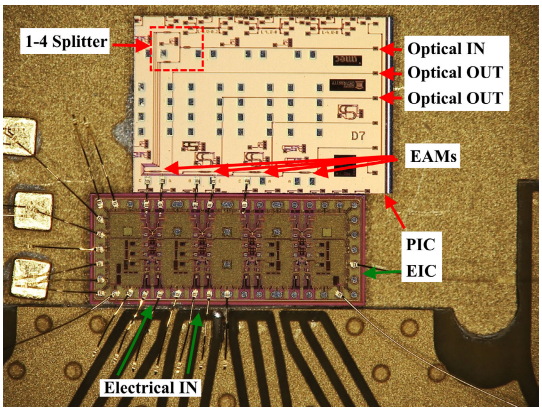

(a)

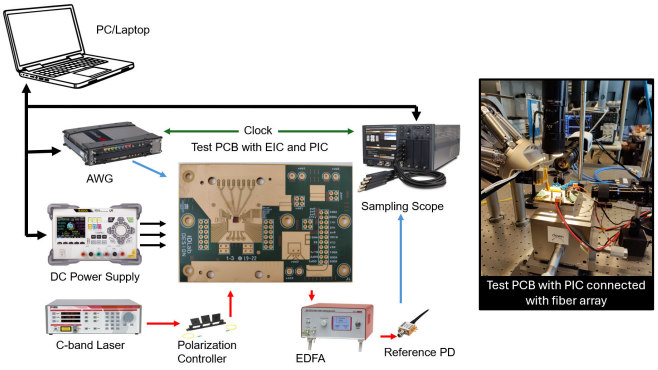

(b)

Fig. 9. Measurement setups for the optical time-domain measurements. (a) Closeup of wire-bonded driver and PIC. (b) Overview.

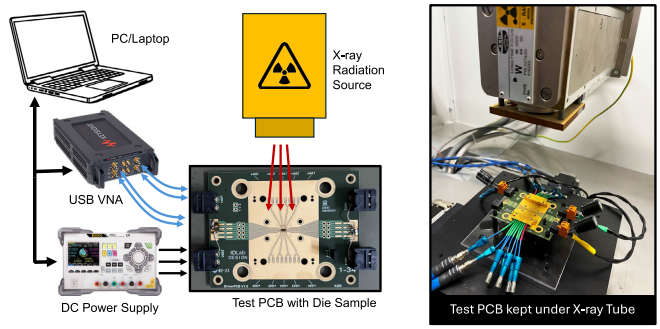

(a)

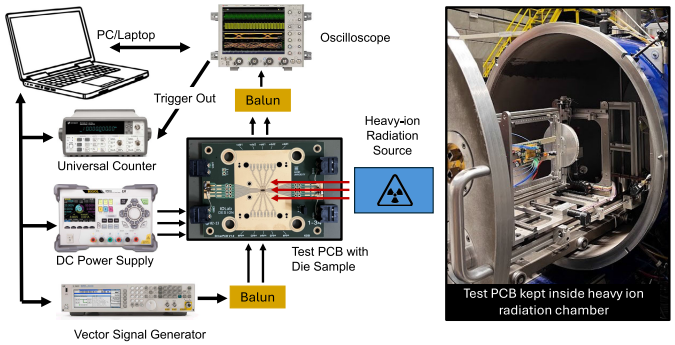

(b)

Fig. 10. Measurement setups for (a) TID measurement and (b) SEE measurement.

heavy-ion test setup can be seen in Fig. 10(b). The cyclotron had accelerated heavy ions in a range of LETs from 20.4 to

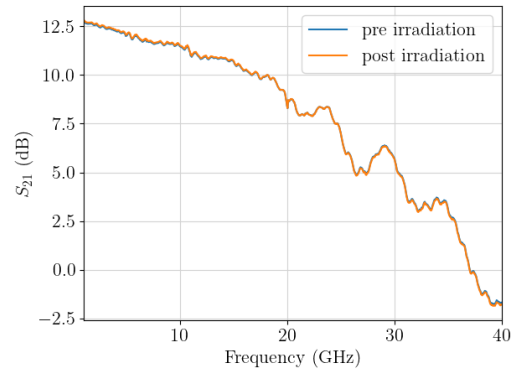

(a)

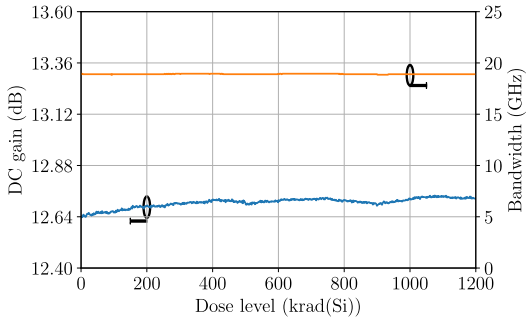

(b)

Fig. 11. (a) Frequency response of the driver including PCB traces and the TR-70 connector before and after 1.2-Mrad(Si) irradiation. (b) Evolution of the dc gain and bandwidth with the dose level.

65.2 MeV cm^2/mg (^{58}Ni^{18+}, ^{84}Kr^{25+}, ^{103}Rh^{31+}, and ^{124}Xe^{35+}). The ion energies were 582, 769, 957, and 995 MeV, respectively. The chip was mounted inside the radiation chamber, under vacuum, and at ambient temperature, and the input was connected using SMA cables to a signal generator, which generates a sine wave of the appropriate input level with a frequency ranging from 10 to 1000 MHz. Although this is much lower than the bandwidth of the fabricated driver, the upper limit of this frequency range is caused by the minimal pulsewidth the real-time oscilloscope (RTO) can trigger. The output was connected to a Keysight DSAZ634A RTO, which was configured to trigger pulses less wide than half the input sine wave period. The trigger output of the RTO was then connected to a universal counter, which thus counts the number of times that SET pulses cross the mid-level, and thus could, at full rate, introduce bit errors. During the test, each sample was irradiated with a flux of 1.5×10^4 particles/s/cm^2 until a fluence of 1.2×10^7 particles/cm^2 was reached.

A snapshot of the SET with the longest pulse duration (5 ns) observed during the measurement can be seen in Fig. 12. The number of SETs counted for different input frequencies and LETs can be seen in Fig. 13. To fit a Weibull distribution [see (2)] to the data points, all measurements where no SETs were observed are ignored, although they were taken into account when calculating the confidence interval as in [54]. The onset is chosen at the highest energy where zero SETs were observed, and the rest of the parameters are fit using a nonlinear least-squares method to the worst case measure-

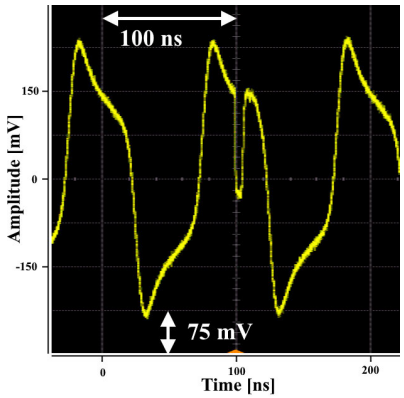

Fig. 12. Closeup of SET event with a 10-MHz input signal.

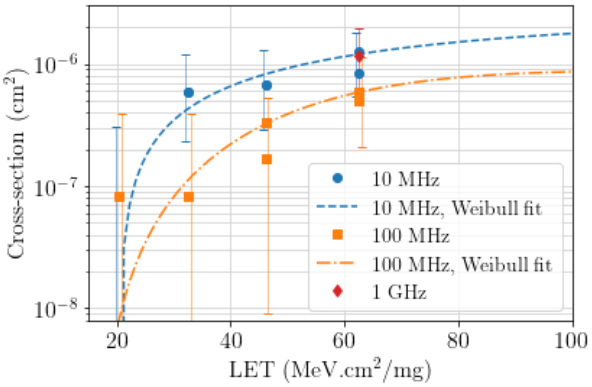

Fig. 13. SET cross section after a fluence of 1.2×10^7 particles/cm^2 has been reached. The error bars are defined by the 95% confidence interval, as in [54]. Lower bound of confidence interval for 20.4 and 32.4 MeV cm^2/mg at 100 MHz is 4×10^{-11} cm^2, and for 20.4 MeV cm^2/mg at 10 MHz, it is 0 cm^2.

TABLE II
WEIBULL PARAMETERS IN FIG. 13 AND MTBE CALCULATION

Parameter	10 MHz fit	100 MHz fit
σ_{sat} [cm^2]	2.39×10^{-6}	8.88×10^{-7}
Onset [MeV cm^2/mg]	20.4	16.1
W [MeV cm^2/mg]	60.9	44.7
s [-]	1	2
Integral flux at onset LET [55][particles/cm^2/day]	8×10^{-3}	1×10^{-2}
MTBE [years]	143000	309000
Estimated Bit Error Rate (BER) [35] at 56 Gbps [-]	6.4×10^{-13}	2.4×10^{-13}

ments for each LET. The fit parameters are summarized in Table II

$$\sigma = \sigma_{\text{sat}}\left(1 - e^{-\left(\frac{\text{LET}-\text{Onset}}{W}\right)^s}\right). \quad (2)$$

To obtain a lower bound for the mean time between events (MTBE), the integral flux at the onset LET, as measured in [55], assuming the LEO orbit, is multiplied by the saturation cross section.

To monitor SELs, the power supply used to bias the samples was recorded, to check whether the current limit of twice the nominal current was reached. No latchup was observed during this experiment.

TABLE III
STATE-OF-THE-ART COMPARISON OF RADIATION-TESTED ELECTRO-OPTICAL TRANSMITTERS FOR SPACE APPLICATIONS

	[30]	[36]	[31]	[32]	This work
Channels	1	1	12	4	4
Targeted device	VCSEL	MZM	VCSEL	VCSEL	SiPh EAM
Bit rate (Gbps)	6.25	10	28	40	56
Extinction Ratio (dB)	-	2.5	5	-	2
Power (mW/ch)	210	115†	314*	100	62.5†
Energy Efficiency(pJ/b)	33.6	11.5†	11.2*	2.5	1.1†
TID tolerance (krad(Si))$^\$$	100	1×10^6	107	100	1200
LET$_{max}$ (MeV cm^2/mg)$^\$$	62	-	66.7	-	65.2
Saturated cross-section (cm^2)	4.8×10^{-4}	-	3.6×10^{-3}	-	2.4×10^{-6}

* Combined power (TX+RX), †Laser power not included. $^\$$Highest tested

V. DISCUSSION

The driver chips were irradiated with X-rays to assess their performance degradation at a TID level of 1.2 Mrad(Si). As shown in Fig. 11, the bandwidth remained consistent throughout the experiment, while the gain exhibited minor variations. Interestingly, a subtle gain increase was observed with increasing TID. This can be attributed to the decrease in the threshold voltage of the n-channel MOSFETs used inside the current mirror circuit to bias the drivers. After irradiation, the samples were subjected to annealing, and no major variations were observed during the process.

The samples were also tested with heavy ions at different LET values. Starting from 20 MeV cm^2/mg, SETs with variable pulse duration were observed, ranging from 0.1 to 5 ns, invariable with an LET. In the worst case, at the full rate of 56 Gb/s, this pulse could introduce a 280-bit-long burst error. This worst case scenario is probably related to the critical node identified in Fig. 4, although further experiments should be done to verify that claim. One possible solution to this problem could be increasing the collector current, such that the driver would be more robust to the increased rise time caused by the change in V_{CE}, as discussed in Section II. However, this would likely require a vast increase in current, which would cause the impressive 1.1-pJ/b energy efficiency to plummet. During the experiment, the maximum number of SETs, 15, was observed with an LET of 65.2 MeV cm^2/mg. However, the calculated lower bound for the MTBE is more than 143 000 years, which means that it is unlikely that an SET will be observed during the lifetime of the satellites.

The estimated bit-error-rate (BER) (as per [35]) values at 56 Gb/s using the optical modulator corresponding to cross section of 2.39×10^{-6} and 8.88×10^{-7} cm^2 are 6.4×10^{-13} and 2.4×10^{-13}, respectively. SELs were not observed during the experiment, which establishes the driver's immunity against latchup events for ion energies less than 65.2 MeV cm^2/mg in vacuum at ambient temperature.

A state-of-the-art comparison of reported electro-optical transmitters for space applications is made in Table III. The VCSEL driver in [30] was implemented in a 130-nm SiGe process and targeted 6.25-Gb/s communication links in satellites. The drivers had been qualified with the space-radiation standards but at the expense of very high power consumption. Compared to [30], the optical driver as reported in [36] achieved a higher bit rate (10 Gb/s) and tested up to a TID level of 1 Grad(Si) while being more power efficient

than [30]. Radiation-hardened optical transceiver modules with 12 parallel channels, achieving 28 Gb/s bit rate per channel were reported in [31]. The four-channel optical driver of [32] achieved 40 Gb/s bit rate per channel. The drivers in [32] and [36] have not been tested with heavy ions, but [32] underwent SEE radiation testing with maximum proton energy levels of 60 MeV. No data related to effective LET values were reported in [32] and [36]. In comparison, this work's optical modulator achieves 1.4 times the bit rate per channel (56 Gb/s) with an energy efficiency of 1.1 pJ/b. Even if the laser power is to be taken into account, which is estimated to be an extra 0.5 pJ/b, energy efficiency is still the best among Table III. To the author's knowledge, this work showcases the best energy efficiency, bit rate, and radiation tolerance in comparison to its counterparts [30], [31], [32], [36] designed for space applications.

VI. Conclusion

This radiation assessment study presents the development and the performance evaluation of a high-speed, radiation-tolerant modulator driver designed for 56-Gb/s EAM applications in intrasatellite optical links. The driver is designed in a radiation-hardened-by-process 130-nm SiGe BiCMOS process and is shown to drive an EAM at speeds up to 74 Gb/s with a power efficiency of 0.9 pJ/b. To assess its performance in a realistic space environment, the driver underwent a comprehensive radiation hardness evaluation. This assessment included X-ray irradiation up to the TID level of 1.2 Mrad(Si) and heavy-ion exposure to evaluate SEE susceptibility across a range of LETs from 20 to 65.2 MeV cm^2/mg with a fluence of 1.2×10^7 cm^{-2}. The TID experiments resulted in a maximum 0.1-dB deviation in the driver's frequency response after 1.2 Mrad(Si) of irradiation, and after a fluence of 1.2×10^7 cm^{-2} of ions with an LET of 65.2 MeV cm^2/mg, only 15 SETs were observed. The driver's functionality remained uninhibited throughout these experiments, and no SEL event was observed, showcasing its significant radiation tolerance. These conclusions validate the suitability of this driver design for future high-bandwidth, reliable intrasatellite optical communication for critical space applications.

Acknowledgment

The authors would like to thank IHP for providing access to the SG13RH process and Keysight Technologies for lending a 40-GHz P5028A VNA.

References

[1] T. Fujisawa et al., "4×25-Gbit/s, 40-km SMF transmission based on 1.3-μm electroabsorption modulators integrated with DFB lasers for 100-Gbit/s Ethernet," in *Opto-Electron. Commun. Conf. (OECC) Tech. Dig.*, Jul. 2010, pp. 50–51.

[2] T. Ohyama et al., "Compact hybrid-integrated 100-Gbit/s TOSA for 40-km transmission," in *Proc. Opto-Electron. Commun. Conf. (OECC)*, Dec. 2015, pp. 60–62.

[3] S. Niu et al., "A linear modulator driver with over 70-GHz bandwidth 21.8-dB gain and 3.4-Vppd output swing for beyond 120-GBd optical links," *IEEE Trans. Microw. Theory Techn.*, vol. 72, no. 7, pp. 4080–4091, Jul. 2024.

[4] K. Bałakier et al., "Photonic integrated circuit technology for communication satellites payloads," in *Proc. 49th Eur. Conf. Opt. Commun. (ECOC)*, Nov. 2023, pp. 1627–1631.

[5] A. L. Vampola, "The hazardous space particle environment," *IEEE Trans. Plasma Sci.*, vol. 28, no. 6, pp. 1831–1839, Dec. 2000.

[6] S. Bourdarie and M. Xapsos, "The near-Earth space radiation environment," *IEEE Trans. Nucl. Sci.*, vol. 55, no. 4, pp. 1810–1832, Aug. 2008.

[7] M. A. Xapsos, P. M. O'Neill, and T. P. O'Brien, "Near-earth space radiation models," *IEEE Trans. Nucl. Sci.*, vol. 60, no. 3, pp. 1691–1705, Jun. 2013.

[8] J. L. Barth, C. S. Dyer, and E. G. Stassinopoulos, "Space, atmospheric, and terrestrial radiation environments," *IEEE Trans. Nucl. Sci.*, vol. 50, no. 3, pp. 466–482, Jun. 2003.

[9] A. Karmakar, J. Wang, J. Prinzie, V. De Smedt, and P. Leroux, "A review of semiconductor based ionising radiation sensors used in harsh radiation environments and their applications," *Radiation*, vol. 1, no. 3, pp. 194–217, Aug. 2021.

[10] I. Jun et al., "A review on radiation environment pathways to impacts: Radiation effects, relevant empirical environment models, and future needs," *Adv. Space Res.*, to be published.

[11] M. A. Xapsos, "Modeling the space radiation environment," presented at the IEEE Nucl. Space Radiat. Effects Conf. Short Course, 2006.

[12] S. Giannakopoulos et al., "A 112 Gb/s radiation-hardened mid-board optical transceiver in 130-nm SiGe BiCMOS for intra-satellite links," *Frontiers Phys.*, vol. 9, May 2021, Art. no. 672941.

[13] J. Lauzon, T. Oleszczak, D. Rolston, R. Varano, S. E. Kharraz, and N. Safdari, "Reliability of connectorized 10 Gbps/channel optical fiber transceivers," in *Proc. IEEE Avionics Vehicle Fiber-Opt. Photon. Conf. (AVFOP)*, Oct. 2016, pp. 277–278.

[14] R. T. Logan et al., "Radiation test results for glenair 5 Gbps and 40 Gbps (4×10 Gbps) optical transceivers," in *Proc. IEEE Radiat. Effects Data Workshop*, Jul. 2019, pp. 101–108.

[15] J. D. Cressler, "Radiation effects in SiGe technology," *IEEE Trans. Nucl. Sci.*, vol. 60, no. 3, pp. 1992–2014, Jun. 2013.

[16] J. Solano et al., "Total ionizing dose response of commercial 22 nm FD-SOI CMOS technology," in *Proc. IEEE Radiat. Effects Data Workshop (REDW)*, Jul. 2022, pp. 100–104.

[17] Y. Yin et al., "Total ionizing dose and single event effect response of 22 nm ultra-thin body and buried oxide fully depleted silicon-on-insulator technology," *Microelectron. Rel.*, vol. 152, Jan. 2024, Art. no. 115296.

[18] G. Termo et al., "Characteristics and ultra-high total ionizing dose response of 22 nm fully depleted silicon-on-insulator," *J. Instrum.*, vol. 19, no. 3, Mar. 2024, Art. no. C03039.

[19] D. M. Fleetwood, "Evolution of total ionizing dose effects in MOS devices with Moore's law scaling," *IEEE Trans. Nucl. Sci.*, vol. 65, no. 8, pp. 1465–1481, Aug. 2018.

[20] D. Kobayashi, "Scaling trends of digital single-event effects: A survey of SEU and SET parameters and comparison with transistor performance," *IEEE Trans. Nucl. Sci.*, vol. 68, no. 2, pp. 124–148, Feb. 2021.

[21] N. E. Lourenco et al., "The impact of technology scaling on the single-event transient response of SiGe HBTs," *IEEE Trans. Nucl. Sci.*, vol. 64, no. 1, pp. 406–414, Jan. 2017.

[22] A. Ildefonso et al., "Tradeoffs between RF performance and SET robustness in low-noise amplifiers in a complementary SiGe BiCMOS platform," *IEEE Trans. Nucl. Sci.*, vol. 67, no. 7, pp. 1521–1529, Jul. 2020.

[23] S. S. El Nasr-Storey et al., "Effect of radiation on a Mach–Zehnder interferometer silicon modulator for HL-LHC data transmission applications," *IEEE Trans. Nucl. Sci.*, vol. 62, no. 1, pp. 329–335, Feb. 2015.

[24] M. Zeiler et al., "Radiation damage in silicon photonic Mach–Zehnder modulators and photodiodes," *IEEE Trans. Nucl. Sci.*, vol. 64, no. 11, pp. 2794–2801, Nov. 2017.

[25] P. S. Goley et al., "Total ionizing dose effects in 70-GHz bandwidth photodiodes in a SiGe integrated photonics platform," *IEEE Trans. Nucl. Sci.*, vol. 66, no. 1, pp. 125–133, Jan. 2019.

[26] S. Cammarata, F. Palla, S. Saponara, F. Di Pasquale, P. Velha, and S. Faralli, "Compact silicon photonic Mach–Zehnder modulators for high-energy physics," *J. Instrum.*, vol. 19, no. 3, Mar. 2024, Art. no. C03009.

[27] G. N. Tzintzarov et al., "Electronic-to-photonic single-event transient propagation in a segmented Mach–Zehnder modulator in a Si/SiGe integrated photonics platform," *IEEE Trans. Nucl. Sci.*, vol. 67, no. 1, pp. 260–267, Jan. 2020.

[28] P. Leroux et al., "Design and assessment of a circuit and layout level radiation hardened CMOS VCSEL driver," *IEEE Trans. Nucl. Sci.*, vol. 54, no. 4, pp. 1055–1060, Aug. 2007.

[29] G. Mazza et al., "High-speed, radiation-tolerant laser drivers in 0.13 μm CMOS technology for HEP applications," *IEEE Trans. Nucl. Sci.*, vol. 61, no. 6, pp. 3653–3659, Dec. 2014.

[30] A. Tanskanen, M. Karppinen, C. B. Polo, R. J. E. Jansen, and I. McKenzie, "Radiation tolerant 6.25 Gbps 850 nm optical transceiver," in *Proc. 17th Eur. Conf. Radiat. Effects Compon. Syst. (RADECS)*, Oct. 2017, pp. 532–535.

[31] N. Safdari, G. Monette, J. Beydoun, A. Martin, R. Varano, and F. Laforce, "Reliability testing of 28 Gbps/channel fiber optics transceivers for space applications," in *Proc. Int. SpaceWire SpaceFibre Conf. (ISC)*, Oct. 2022, pp. 113–120.

[32] I. Sourikopoulos et al., "A 40Gb/s rad-hard quad VCSEL driver integrated circuit in 130 nm SiGe BiCMOS for intra-satellite optical interconnects," in *Proc. 15th Int. Conf. Space Opt. (ICSO)*, to be published.

[33] S. Cammarata et al., "Design and performance evaluation of multi-Gb/s silicon photonics transmitters for high energy physics," *Energies*, vol. 13, no. 14, p. 3569, Jul. 2020.

[34] G. Ciarpi, G. Magazzù, F. Palla, and S. Saponara, "Design of radiation-hard MZM drivers," in *Proc. 20th Italian Nat. Conf. Photonic Technol. (Fotonica)*, May 2018, pp. 100–104.

[35] G. Ciarpi, G. Magazzù, F. Palla, and S. Saponara, "Design, implementation, and experimental verification of 5 Gbps, 800 Mrad TID and SEU-tolerant optical modulators drivers," *IEEE Trans. Circuits Syst. I, Reg. Papers*, vol. 67, no. 3, pp. 829–838, Mar. 2020.

[36] G. Ciarpi et al., "Design and characterization of 10 Gb/s and 1 Grad TID-tolerant optical modulator driver," *IEEE Trans. Circuits Syst. I, Reg. Papers*, vol. 69, no. 8, pp. 3177–3189, Aug. 2022.

[37] S. S. Azadeh et al., "Low V_π Silicon photonics modulators with highly linear epitaxially grown phase shifters," *Opt. Exp.*, vol. 23, no. 18, pp. 23526–23550, Sep. 2015.

[38] J. Witzens, "High-speed silicon photonics modulators," *Proc. IEEE*, vol. 106, no. 12, pp. 2158–2182, Dec. 2018.

[39] G. Ghione, *Semiconductor Devices for High-Speed Optoelectronics*. Cambridge, U.K.: Cambridge Univ. Press, 2009.

[40] M. Pantouvaki et al., "Active components for 50 Gb/s NRZ-OOK optical interconnects in a silicon photonics platform," *J. Lightw. Technol.*, vol. 35, no. 4, pp. 631–638, Feb. 15, 2017.

[41] M. Krstic, J. Schmidt, A. Breitenreiter, F. Teply, and R. Sorge, "Evaluierung einer strahlungsharten bibliothek in 0.13 μm BiCMOS," in *Proc. DLR Bauteilekonferenz*. ULM, Apr. 2018.

[42] E. Säckinger, *Broadband Circuits for Optical Fiber Communication*. Hoboken, NJ, USA: Wiley, 2005.

[43] H. Ramon et al., "70 Gb/s low-power DC-coupled NRZ differential electro-absorption modulator driver in 55 nm SiGe BiCMOS," *J. Lightw. Technol.*, vol. 37, no. 5, pp. 1504–1514, Mar. 1, 2019.

[44] S. J. Gaul, N. van Vonno, S. H. Voldman, and W. H. Morris, *Integrated Circuit Design for Radiation Environments*. Hoboken, NJ, USA: Wiley, 2019.

[45] M. A. R. Sarker et al., "Mitigation of single-event effects in SiGe-HBT current-mode logic circuits," *Sensors*, vol. 20, no. 9, p. 2581, May 2020.

[46] G. C. Messenger, "Collection of charge on junction nodes from ion tracks," *IEEE Trans. Nucl. Sci.*, vol. NS-29, no. 6, pp. 2024–2031, Dec. 1982.

[47] D. Monda, G. Ciarpi, and S. Saponara, "Analysis and comparison of rad-hard ring and LC-tank controlled oscillators in 65 nm for SpaceFibre applications," *Sensors*, vol. 20, no. 16, p. 4612, Aug. 2020.

[48] M. Andjelkovic, M. Krstic, and R. Kraemer, "Comparison of the SET sensitivity of standard logic gates designed in 130 nm CMOS technology," in *Proc. IEEE 30th Int. Conf. Microelectron. (MIEL)*, Oct. 2017, pp. 217–220.

[49] L. W. Massengill, M. L. Alles, and S. E. Kerns, "SEU error rates in advanced digital CMOS," in *Proc. 2nd Eur. Conf. Radiat. Effects Compon. Syst.*, 1993, pp. 546–553.

[50] C. T. Kirk, "A theory of transistor cutoff frequency (fT) falloff at high current densities," *IRE Trans. Electron Devices*, vol. 9, no. 2, pp. 164–174, Mar. 1962.

[51] J. D. Cressler, *Silicon-Germanium Heterojunction Bipolar Transistors*. Norwood, MA, USA: Artech House, 2002.

[52] Z. E. Fleetwood et al., "SiGe HBT profiles with enhanced inverse-mode operation and their impact on single-event transients," *IEEE Trans. Nucl. Sci.*, vol. 65, no. 1, pp. 399–406, Jan. 2018.

[53] O. Gutiérrez, M. Prieto, A. Perales-Eceiza, A. Ravanbakhsh, M. Basile, and D. Guzmán, "Toward the use of electronic commercial off-the-shelf devices in space: Assessment of the true radiation environment in low Earth orbit (LEO)," *Electronics*, vol. 12, no. 19, p. 4058, Sep. 2023.

[54] *Single Event Effects Test Method and Guidelines, ESCC Basic Specification, No. 25100*, Eur. Space Components Coordination (ESCC), Noordwijk, The Netherlands, Jun. 2014.

[55] X. Liang et al., "Impact of heavy-ion irradiation on gate oxide reliability of silicon carbide power MOSFET," *Radiat. Effects Defects Solids*, vol. 176, nos. 11–12, pp. 1038–1048, Nov. 2021.